Journal of Civil Structural Health Monitoring (2025) 15:227–244
https://doi.org/10.1007/s13349-024-00823-8

ORIGINAL PAPER

Code-specified early delamination detection and quantification in a RC bridge deck: passive vs. active infrared thermography

Haibin Zhang[1,2] · Zhenhua Shi[1] · Liujun Li[1,3] · Pu Jiao[1] · Bo Shang[1] · Genda Chen[1]

Received: 1 January 2024 / Accepted: 23 June 2024 / Published online: 6 August 2024
© Springer-Verlag GmbH Germany, part of Springer Nature 2024

Abstract

Delamination in reinforced concrete (RC) bridge decks can degrade the serviceability of entire bridges, leading to concrete spalling and steel rebar corrosion and eventually becoming a safety concern. Drone-based infrared thermography (IRT) offers a promising tool for rapid assessment of bridge deck delamination compared to labor-intensive coring and visual inspection methods. However, the performance of passive IRT in detecting the delamination of RC bridge decks at its minimum depth and size (i.e., spall 25 mm or less deep or 150 mm or less in diameter) stipulated under a 'fair' condition state in the 2019 AASHTO Manual for Bridge Element Inspection has not been verified adequately. In this study, four RC slabs of identical design were cast with embedded thin foam sheets to simulate a wide range of delamination in thickness, size, spacing, and depth. Together, the four slabs form a representative RC deck of a mark-up bridge. Controllable indoor active IRT tests of individual slabs were conducted to detect and quantify the foams that serve as a ground truth for the performance of drone-based passive IRT for deck delamination detection on the mark-up bridge as the embedded foams may be displaced during concrete slab casting and the slab support is altered during erection. Statistical analysis was carried out on the thermal contrasts of both passive and active IRT tests on the four slabs to investigate the effects of delamination geometry and embedment depth. Both the active and passive IRT methods proved successful in localizing delamination and identifying its equivalent thicknesses of as low as 1.63 mm and a size (150 mm in length or 25 mm in depth) corresponding to the 'fair' condition state in the AASHTO Manual for Bridge Element Inspection.

Highlights

1. Statistical analysis is conducted to assess the capabilities of IRT in delamination detection.
2. Active IRT tests are introduced to evaluate the performance of UAV-based passive IRT.
3. Thickness, size, spacing, and depth of delamination are considered in parametric study.
4. Thermal contrast and gradient amplitude are employed to quantify delamination.

Keywords Non-destructive evaluation (NDE) · Unmanned aerial vehicle (UAV) · Infrared thermography (IRT) · Reinforced concrete (RC) · Bridge decks · Delamination

✉ Genda Chen
gchen@mst.edu

[1] Department of Civil, Architectural, and Environmental Engineering, Missouri University of Science and Technology, Rolla 65401, USA

[2] School of Civil Engineering and Architecture, Hainan University, Haikou 570228, China

[3] College of Agricultural and Life Sciences, University of Idaho, Moscow 83844, USA

1 Introduction

The deterioration of aging infrastructure poses a potential threat to the safety of the public. As reported by the American Road & Transportation Builders Association [1], more than 30% of bridges in the United States need replacement or rehabilitation. Among all reinforced concrete (RC) bridge components, bridge decks have been identified as the most problematic due to their susceptibility to various deterioration mechanisms [2]. Despite representing a small portion of

the initial expenditure for bridges, the RC decks account for 50 to 85% of annual bridge maintenance investment or up to $125 billion in the United States [3, 4]. To manage costs and ensure the public safety, the federal government mandates periodic inspections on all bridges along the interstate and U.S. highways with inspection intervals ranging from 12 to 48 months based on factors such as bridge condition, type, traffic, location, and age [2, 4].

RC bridge deck deterioration may start in unbonded subsurfaces and unintegrated interiors, including delamination and cracking [2]. Concrete delamination occurs in the cover of RC members near their surface due to the expansion of corroded embedded rebar, environmental variations, and cyclic traffic loads. If repairs are not made in a timely fashion, delamination can lead to further deterioration and spalling [5, 6], eventually compromising the structural integrity of the deck. Currently, the most common methods for bridge evaluation are physical (e.g., coring) and visual inspections. However, these methods suffer from drawbacks such as high subjectivity, dependence on skills or experiences, and limited accessibility [7, 8]. Moreover, these assessments often require traffic control or lane closures.

Non-destructive testing (NDT) technologies provide an effective means of monitoring the subsurface deterioration of RC bridge decks. Among various NDT methods, infrared thermography (IRT) has gained widespread popularity due to its real-time, low-cost, non-contact, and wide-area measurement advantages [9, 10]. IRT involves measuring infrared radiation, which corresponds to the surface temperature distribution collected by a thermal camera. This data can be interpreted to determine the dimensions of delamination in the bridge structure. To improve the efficiency of delamination detection while minimizing traffic disruption, unmanned aerial vehicle (UAV) equipped with thermal cameras represents a cost-effective and valuable option for inspecting hard-to-reach areas of bridges. This method has increasingly attracted the interest of state and local transportation authorities and stakeholders, and significant efforts have been devoted to using UAVs with IRT for detecting delamination in RC bridge decks [11–15]. However, the manual operation of UAVs requires the availability of skillful, well-trained pilots and, even then, involves a risk of potential incidents. Therefore, autonomous UAVs were recommended in practical applications. With the help of advanced machine learning, automatic bridge damage detection can be achieved more effectively and efficiently [16–20]. Real-time multiple damage mapping using an autonomous UAV and deep faster region-based neural networks for GPS-denied structures was reported to show a favorable precision of 93% in average for damage detection in large-scale RC structures [20].

According to AASHTO's manual for bridge element inspection [21], the classification of a RC bridge deck's health condition depends not only on the size but also on the embedment depth of delamination. For instance, a spall 1 inch or less in depth or 6 inches or less in diameter is considered to be a fair condition. If the parameter exceeds this threshold, it is classified as being in a poor or even severe condition. Two types of impact factors affect the performance of IRT, including environmental conditions and thermal properties of detected objects [22]. Instead of on-site tests, to access the capabilities of IRT for detecting delamination in RC bridge deck, more controllable laboratory studies were widely carried out to minimize the influence of environmental conditions [11, 23–29]. These studies adopted artificial materials to mimic delamination that expected to represent the behavior of an actual delamination.

Delaminated concrete is anticipated to have less density and more air voids than sound concrete, and thus, low-density styrofoam has been extensively employed as a suitable simulation material for delamination. According to the numerical studies conducted by Hiasa et al. [26], the performance of delamination detection using IRT is influenced not only by the delamination size and depth but also by the thickness of delamination. Previous experimental studies have mainly focused on investigating the detection capabilities of IRT in terms of defect size and depth, overlooking the importance of thickness. Moreover, some studies used a foam thickness of 40–50 cm [27–29], which is not representative of actual delamination dimensions. To timely and efficiently identify delamination, the performance of UAV-based passive IRT for detecting small and shallow delamination should be investigated. Therefore, there is a need to further explore the capabilities of IRT in identifying deterioration in RC bridges through simulated small defects, as it can provide more in-depth insights into the resolution of IR imaging. This, in turn, can help prevent significant repair expenses and offer a range of decision-making options.

This paper aims to investigate the capabilities of passive IRT in timely and rapidly detecting the delamination of a mockup bridge deck consisting of four RC slabs. The thickness, size, spacing, and depth factors are considered. To mitigate the influence of environmental conditions, controlled laboratory tests are conducted using active IRT. The active IRT results provide "ground truth" for verification and validation of the passive IRT in situ tests in the open field. Statistical analysis is performed on the four individual RC slabs with a variety of small delamination sizes. Thermal contrast is employed to investigate the effects of delamination properties on the detectability of delamination using IRT. The algorithm involving temperature gradients is adopted to quantify the delamination size. The results obtained from the active IRT were compared with those of UAV-based passive IRT to verify its performance in delamination detection.

2 Fundamentals on the use of IRT

The fundamentals on the use of IRT is introduced in this section. They include underlying theory, impact factors, delamination detection, and evaluation and verification methods.

2.1 The underlying theory

The principle of IRT for bridge delamination inspection is based on the difference in heat transfer between sound and delaminated materials in the subsurface of a bridge deck. Heat energy can be transferred through three ways: conduction, convection, and radiation. The wavelength of radiation approximately ranges from 1 μm to 1000 μm, which is known as the infrared range. Infrared radiation is emitted by objects at temperatures above absolute zero, i.e., − 273.15 °C (0 Kelvin). The radiation energy can be measured by an infrared camera, as it is a function of their temperature and emissivity, as presented in Eq. (1) [30].

$$E = \varepsilon \sigma T^4, \tag{1}$$

where E = total radiant energy emitted from an object's surface, ε = emissivity of the object, σ = Stefan–Boltzmann constant (5.67×10^{-12} W/cm^{2}k^4), and T = absolute temperature of the emitting object in Kelvin.

The emissivity refers to the ability of an object's surface to emit energy by radiation relative to a perfect blackbody with an emissivity of unity. It ranges from 0 for no emission to 1 for a perfect emitter. The emissivity of concrete is relatively high and typically larger than 0.92 [30]. Consequently, concrete is a good emitter of heat compared to other materials, such as metals.

During the monitoring process of both active and passive IRT, transient heat diffusion occurs, which is related to the thermal properties of the materials and the heat source [31], as follows:

$$\rho c \frac{\partial T(x,t)}{\partial t} = k \frac{\partial T^2(x,t)}{\partial x^2} + Q, \tag{2}$$

in which ρ = material density, c = specific heat, t = heating or cooling time, x = coordinate of spatial position, k = thermal conductivity, Q = energy input, and T = absolute temperature as a function of space and time.

When the thermal conduction is stabilized, the following equation applies.

$$\Delta T_{i,i+1} = QR_i, \tag{3}$$

where $\Delta T_{i,i+1}$ = the temperature difference between layer i and $i+1$ of the material, and R_i = thermal resistance, which can be expressed into:

$$R_i = \frac{d_i}{k_i A_i}, \tag{4}$$

in which d_i = thickness of the i^{th} layer material, k_i = thermal conductivity of the ith layer material, and A_i = area of the i^{th} layer material. Equation (4) indicates that the temperature difference increases with the layer thickness and decreases with the thermal conductivity and area. In delamination detection, the layer thickness correlates not only with the concrete depth on top of the delamination [24, 25, 28] but also with the delamination thickness itself [25]. This information is crucial in understanding the factors that influence the temperature difference and can be valuable in the effective detection of delamination in bridge decks using infrared thermography.

2.2 Impact factors

Besides the thermal properties of an object to be detected, as demonstrated in Eq. (4), the detectability of delamination from an IRT depends upon surface characteristics of the object, such as oil stain, texture, color, and roughness [12, 32]. In addition, environmental conditions significantly affect the performance of thermal imaging, including ambient temperature, wind speed, humidity, and solar loading. According to American Society for Testing and Materials (ASTM), IRT should not be carried out when the ambient temperature is below 0 °C (32 °F) to avoid false delamination readings caused by ice [33]. Furthermore, delamination detection is unsuitable when wind speed exceeds 50 kph (30 mph), as the thermal contrast between delaminated and sound regions decreases with the wind speed due to surface temperature shear effects [33, 34]. Many studies have applied the ASTM standards during data collection at bridge sites for delamination detection from IRT [32, 35]. Moreover, humidity, rain or snow can reduce the measured temperature values and thermal contrast due to the endothermic reaction induced by water evaporation, resulting in local surface cooling [36]. Solar loading also affects thermal imaging results as low solar intensity or periodic cloud cover can significantly delay the observation of subsurface features in thermal images [28].

2.3 Delamination detection

IRT can be divided into two categories: active and passive, based on the requirement of externally supplied energy. Active IRT involves the application of a non-natural energy source (such as microwave, eddy current, and laser) to the inspected regions while collecting data during heating or cooling phases [23, 24, 37]. On the other hand, passive IRT utilizes the natural energy sources (such as solar and ambient temperature variation) to stimulate temperature distribution

in the inspected structures [11, 12, 38]. While the active IRT can detect smaller defects and provide more detailed information about the defect characteristics compared to the passive IRT, it is often more expensive to implement for large-scale infrastructure due to the limited area that an external heating source can cover. In contrast, the passive IRT is commonly employed for detecting the delamination of RC bridge decks in practical applications. Table 1 summarizes the pros and cons of active and passive IRT methods for the detection of RC bridge deck delamination.

Figure 1 shows a schematic view of RC deck delamination detection using passive (daytime when subjected to natural solar radiation) and active IRT (immediately after a non-natural heat source removed), respectively. When a delamination layer occurs in concrete, which could initiate from debonding between concrete and multiple steel bars, air occupies the space formed by the delamination and, thus, reduces the thermal conductivity of the deteriorated region. As a result, the solar heat conduction in the delamination region is less efficient than its surrounding sound region, causing higher radiation heat and temperature on the top surface of the delaminated region [39]. Similarly, when a non-natural heat source is removed, the heat trapped in the delamination region will radiate more slowly than that in its surrounding sound region. However, the active IRT involving a non-natural heat source is fully controllable while the passive IRT largely depends on the sunlight condition.

Table 1 Comparison between active and passive IRT for concrete delamination detection [26, 32, 38]

	Active IRT	Passive IRT
Pros	High in accuracy Good for depth/size/location determination Independent of weather condition Applicable to all bridge elements	Large in monitoring area from each test No heating boundary effect Time efficient No traffic control during inspection using a drone
Cons	Limited in monitoring area from each test Labor intensive Sensitive to boundary effect of a heat source Time consuming	Difficult in depth determination Moderate in accuracy Dependent of solar light or weather condition Susceptible to oil stains or other confusing factors

2.4 Evaluation and verification methods

The thermal test results obtained from both controllably active and rapidly passive IRTs are compared. Two evaluation methods, namely thermal contrast and gradient amplitude, are employed to assess and verify the effectiveness of UAV-based passive IRT.

2.4.1 Time-series thermal contrast

To analyze the thermal profiles, the thermal contrast (ΔT) is introduced as shown in Eq. (5).

$$\Delta T(t) = T\left(x_d, y_d, t\right) - T\left(x_s, y_s, t\right), \tag{5}$$

where $\Delta T(t)$ is the temperature difference at time t, $T(x_d, y_d, t)$ is the measured temperature right above the delaminated location at time t, and $T(x_s, y_s, t)$ is the measured temperature of sounding location at time t. Time zero is defined as the beginning of a cooling phase after the removal of a strip heater in the active IRT. A schematic view of the thermal analysis process is illustrated in Fig. 2. The ΔT at each time instant is analyzed and compared to evaluate the evolution of the temperature distribution in each specimen.

The thermal contrast is obtained from each delamination area in RC slabs using the same process. This process allows for determining the maximum time-varying thermal contrast for each delamination area relative to a reference point in the sound area, thereby establishing the

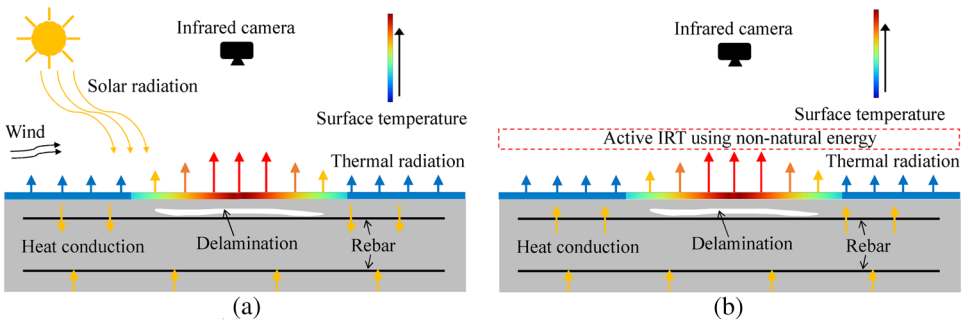

Fig. 1 Schematic view of **a** passive IRT on a RC deck (daytime), and **b** active IRT immediately after a non-natural heat source is removed

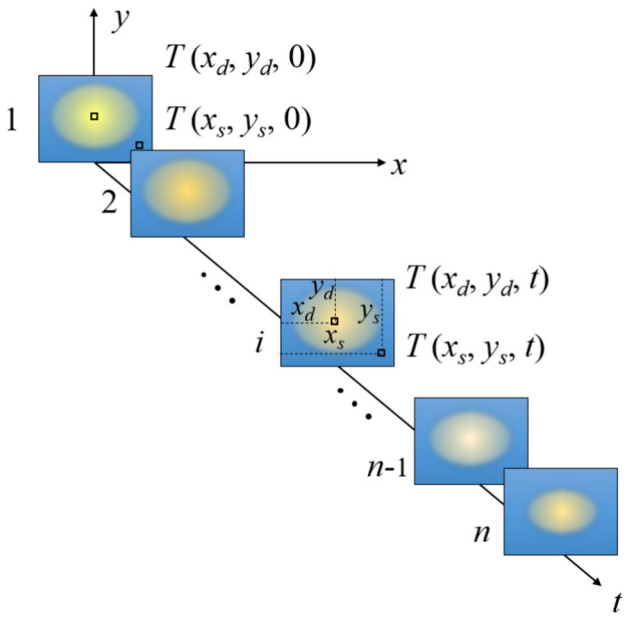

Fig. 2 Illustration of the thermal analysis process

relationship between the delamination depth and size in thermal images. To ensure uniform surface temperature measurements, the reference point is selected at a minimum distance of 102 mm from the edges of both the sound area and the delamination area, as indicated in a previous study [28]. In this study, a reference point 127 mm (5 in.) away from the edges is selected to ensure that the collected data are not influenced by edge effects.

2.4.2 Gradient amplitude

Image gradient is widely used to extract information from an image. Its primary application is in edge detection. In this study, the image gradient is introduced for delamination quantification. The gradient of the image intensity function at each pixel in an image is represented by a two-dimensional (2D) vector with two components given by the derivatives in horizontal (x) and vertical (y) directions. Mathematically, the gradient of an image is defined as shown in Eq. (6).

$$\nabla f = \begin{bmatrix} g_x \\ g_y \end{bmatrix} = \begin{bmatrix} \frac{\partial f}{\partial x} \\ \frac{\partial f}{\partial y} \end{bmatrix}, \tag{6}$$

where $\partial f/\partial x$ and $\partial f/\partial y$ are the partial derivative with respect to x and y (gradient in the x and y directions), respectively. In this study, Prewitt operator [40] is adopted for the edge detection of delamination area. The g_x and g_y can be expressed into:

$$\begin{cases} g_x = \begin{bmatrix} 1 & 0 & -1 \\ 1 & 0 & -1 \\ 1 & 0 & -1 \end{bmatrix} * A, \\ g_y = \begin{bmatrix} 1 & 1 & 1 \\ 0 & 0 & 0 \\ -1 & -1 & -1 \end{bmatrix} * A, \end{cases} \tag{7}$$

where A represents the area of the image. At each pixel in the image, the resulting gradient approximations can be combined to give the gradient magnitude, using Eq. (8)

$$g = \sqrt{g_x^2 + g_y^2}. \tag{8}$$

The gradient magnitudes of all the pixels form a gradient map of the image. The local maximum in gradient magnitude forms a closed loop in the gradient map, the edge of an object causing a significant temperature change from inside to outside of the loop. The area of the closed loop is, thus, indicative of the area of uniform temperature. In this study, the closed-loop area is a result of either the delamination foam board in both active and passive IRTs or the strip heater in the active IRT. Therefore, the close loop represents the corresponding delamination area or the strip heater size.

3 Experimental methods

In this section, the detail of the experimental methods are introduced. They include the design of specimens, and equipment and test setup.

3.1 Design of specimens

Four identical RC slabs, labeled as S1–S4, were designed and cast to assess the effectiveness of the IRT technology for delamination detection. As illustrated in Fig. 3, each specimen measures 182.9 cm (6 ft) in length, 114.3 cm (3.75 ft) in width, and 18.4 cm (7.25 inches) in height. The longitudinal and transverse steel rebars have a diameter of 1 cm (3/8 inch). Commercial mix-ready concrete with an average 28-day compressive strength of 31.5 MPa (4.57 ksi) was used.

Delamination in each RC slab was designed in reference to the AASHTO's Manual for Bridge Element Inspection [21]. According to the Manual, the condition of an RC bridge deck is considered "poor" if delamination exceeds 1 inch (25.4 mm) in depth or 6 inches (15.2 mm) in diameter. To simulate this level of delamination, two types of defects were incorporated into each specimen, referred to as "large" and "small" delamination sheets. For each specimen, six delamination sheets labeled as A to F and six delamination sheets as A′ to F′ were, respectively, positioned at

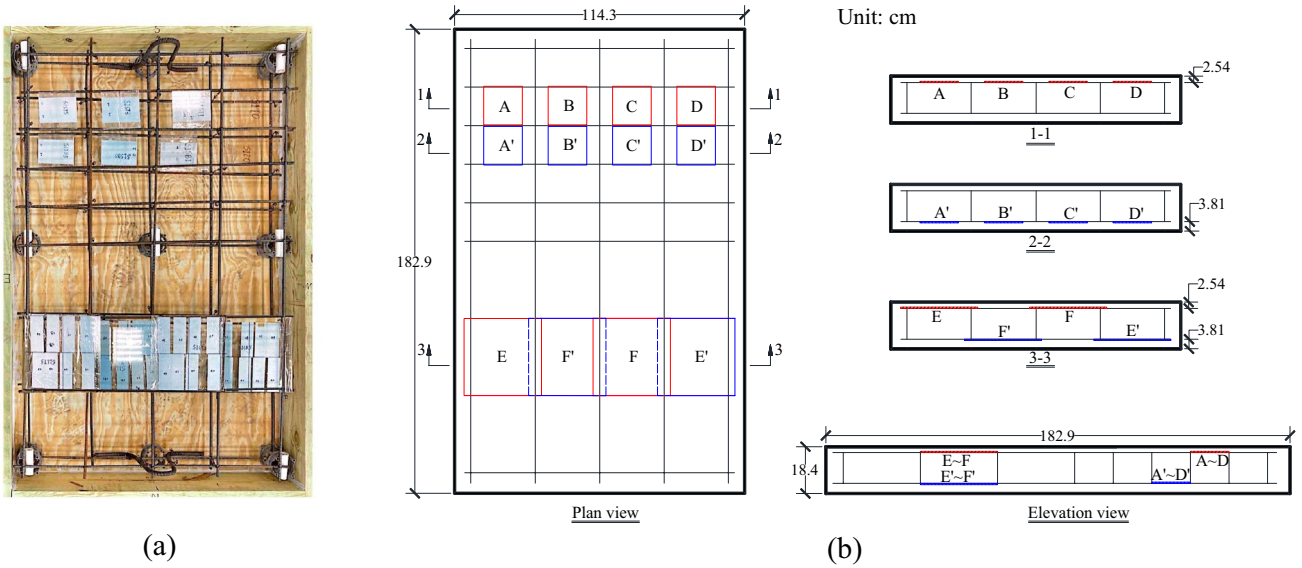

Fig. 3 Details of the specimen and embedded delamination sheets: **a** photo, and **b** sketches

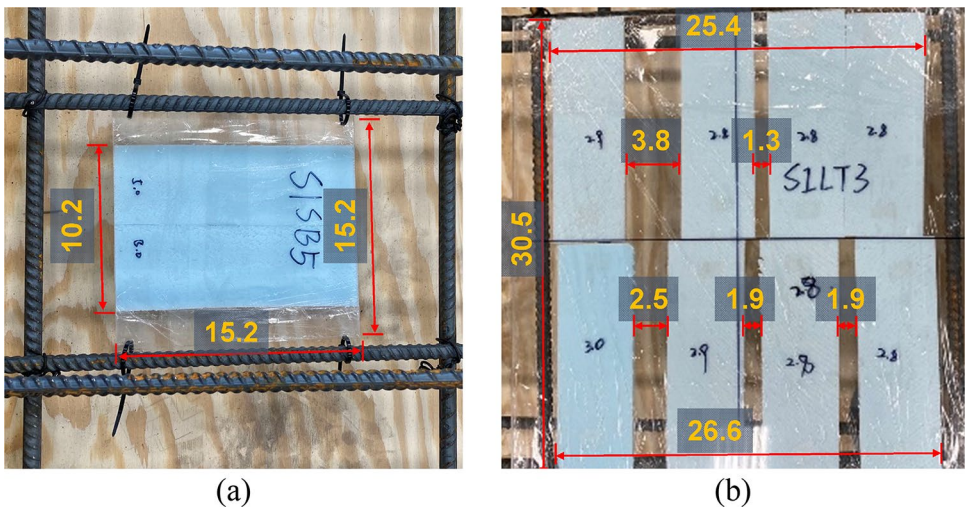

Fig. 4 Styrofoams used in: **a** small and **b** large delamination. (Unit: cm)

depths of 1.0 and 1.5 inches (25.4 and 38.1 mm) from the top and bottom surfaces of the specimen. These depths represent typical concrete cover thicknesses found in RC bridge decks. The small delamination sheet measures 6 × 6 inches (15.2 × 15.2 cm), while the large delamination sheet measures 12 × 12 inches (30.5 × 30.5 cm).

As demonstrated in Fig. 4, all delamination sheets were simulated using a combination of styrofoam strips and a plastic board. The thermal properties of the foam strips were chosen to resemble those of air, replicating the gap between the concrete and rebar caused by rebar corrosion in RC bridge decks. The plastic board serves as a base to support the thin styrofoam strips and prevent them from distortion during concrete casting. The thermal properties of the materials are summarized in Table 2. Each strip has a width equal to the maximum thickness of commercially available styrofoam boards, which is 5.1 cm (2 in.). The

Table 2 Thermal properties of materials

Material	k (W/m K)	c (J/g K)	ρ (kg/m^3)
Concrete	2.006	1.807	2600.00
Steel rebar	45.000	3.500	7850.00
Plastic board	0.213	1.274	1100.00
Styrofoam board	0.024	0.025	25.00
Air	0.025	1.000	1.22

Table 3 Delamination details

Delamination type	Size (cm^2)	Spacing (mm)	Thickness (mm)	Depth (mm)
Styrofoam for small delamination	15.2×5.1	0	0, 1, 3, 5	25.4, 38.1
Styrofoam for large delamination	15.2×5.1	13, 19, 25, 38	3, 5	25.4, 38.1
Plastic for small delamination	15.2×15.2	10.5	8	25.4, 38.1
Plastic for large delamination	30.5×30.5	22.0	8	25.4, 38.1

Table 4 FLIR Duo Pro R specifications

Parameters	Visible imager	Thermal imager
Focal length (mm)	8	13
Fields of view (H×V)	56 °×45 °	45 °×37 °
Resolution	4000×3000	640×512
Spectral band (μm)	0.4–0.7	7.5–13.5

length of each strip matches that of a small plastic board, measuring 15.2 cm (6 in.).

As depicted in Fig. 4a, each small delamination sheet consists of two strips placed side by side without spacing. The foam thicknesses for the small delamination corresponding to A/A′, B/B′, C/C′, and D/D′ as illustrated in Fig. 3 are 5, 3, 1, and 0 mm, respectively. In Fig. 4b, each large delamination is composed of a large plastic board supporting eight strips arranged side by side and spaced by 1.3, 1.9, 2.5, and 3.8 cm, to examine the impact of spacing on IRT. Two different strip thicknesses, 5 and 3 mm (13/64 and 1/8 in.), denoted were used for the large delamination corresponding to E/E′ and F/F′ in Fig. 3, respectively. Further details regarding the delamination sheets are provided in Table 3.

According to Eq. (4), the thermal resistances of 1-, 3-, and 5-mm-thick styrofoams are 0.27, 0.81, and 1.35, respectively. These values are larger than those of 8-mm-thick plastics and concrete, which are 0.17 and 0.017, respectively. This means that the effect of an 8-mm-thick plastic layer is equivalent to that of a styrofoam layer with a thickness of 0.63 mm in terms of heat conduction.

3.2 Equipment and test setup

3.2.1 Thermal camera

FLIR Duo Pro R cameras were used for both active and passive IRT, which is specially designed for use on drones. Each camera comprises a visible imager and a longwave infrared thermal imager. The thermal imager has a sensitivity of 50 mK. Other relevant parameters for both imagers are summarized in Table 4. Among them, the most important parameter is resolution, which will affect the data quality and delamination detection results. However, the higher the image resolution, the greater the camera cost. The selection of cameras reflects a trade-off of resolution and cost.

Fig. 5 Active IRT test setup

3.2.2 Active IRT

As shown in Fig. 5, the heating source used in active IRT was a strip heater measuring 0.3 × 1.2 m (1 × 4 ft). A temperature controller was employed to precisely control the temperature of the strip heater with a sensitivity of ± 4 °C (± 6 °F). To ensure adequate coverage of the area of interest, a top-view (looking down) thermal camera was deployed directly above the heating area at a distance of 213 cm (7 ft). To eliminate any measurement drift, an ice-box was used as a reference at 0 °C (32 °F). The test was conducted inside the Highbay Laboratory at Missouri S&T with air conditioning to minimize the influence of ambient environment. During the data collection period, the room temperature and humidity in the lab were maintained at 20.5 ℃ (69 °F) and 40%, respectively, with a temperature variation of 3 ℃ (5 °F) and a humidity variation of 10%. After the thermal scanning from the top surface was completed, the RC slabs were flipped over to investigate the influence of different delamination embedment depth on active IRT detection. All thermal images were processed using the noise filter function in Matlab to remove noise and enhance clarity. The same test protocol was used for all slabs. That is, the delamination area of each slab was

first heated to 120 °C (250 °F) within 10 min at a heat increasing rate of 40 ℃/min. The heater was then removed and data continued to be collected for another 50 min. The thermal image sampling rate is a constant of 0.05 Hz during both the heating and cooling phases.

3.2.3 Passive IRT

The passive sensing method using solar energy is commonly employed during bridge inspection due to its advantages as presented in Table 1. In this study, an UAV (Model: DJI M600) equipped with a thermal imager was used for passive IRT. The UAV captured thermal images under sunlight from an altitude of approximately 12.2 m (40 ft) above the RC deck on the mark-up bridge, providing a better field of view.

To obtain the most favorable results, the tests were conducted at around 14:00 when the temperature contrast between delamination and sound areas is highest [28]. As shown in Fig. 6, the four RC slabs tested in the Highbay Laboratory were moved to the project site and placed side by side on a steel frame support of two steel girders and four steel columns to form a mark-up girder bridge. This arrangement ensures that data for all the slabs can be collected simultaneously while also eliminating heat conduction from the ground. A weather station was set up on the rear door of a Van to obtain weather information, including wind speed (0.5 m/s), wind direction (Southeast), ambient temperature (25 ℃), and illumination intensity (600 lm/m^2). Additionally, a tarp with three different colors was used to investigate the impact of known material and color on thermal images with the intent of aiding in the image analysis. All thermal images were processed using the same procedure as in active IRT, ensuring consistency in data analysis and comparison.

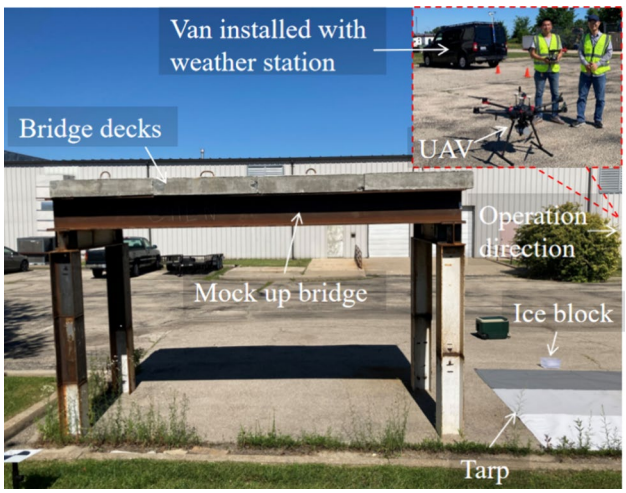

Fig. 6 Passive IRT test setup

4 Experimental results

The experimental results obtained from the active and passive IRTs are demonstrated in this section.

4.1 Active IRT

Figure 7 illustrates the time histories of temperatures at four representative points in one slab specimen. One of these points is located at the center of the strip heater covered area, monitored from the top-view camera. The other three points are situated at distances of 0 mm, 46 mm, and 92 mm below the center of the strip heater covered area on the side face of the specimen. It can be observed that the temperature at the top center position stabilizes after 6 min. Although the temperature of the side concrete surface does not reach the target of 120 ℃ (250 °F), it is significantly higher than the room temperature of 20.5 ℃ (69 °F), creating the necessary temperature difference between delaminated and sounding areas inside the specimens. Upon removal of the heater, the temperature rapidly reduces in about one min and then gradually decreases in the remaining test duration (up to 60 min total). To reduce the data storage space, the total data

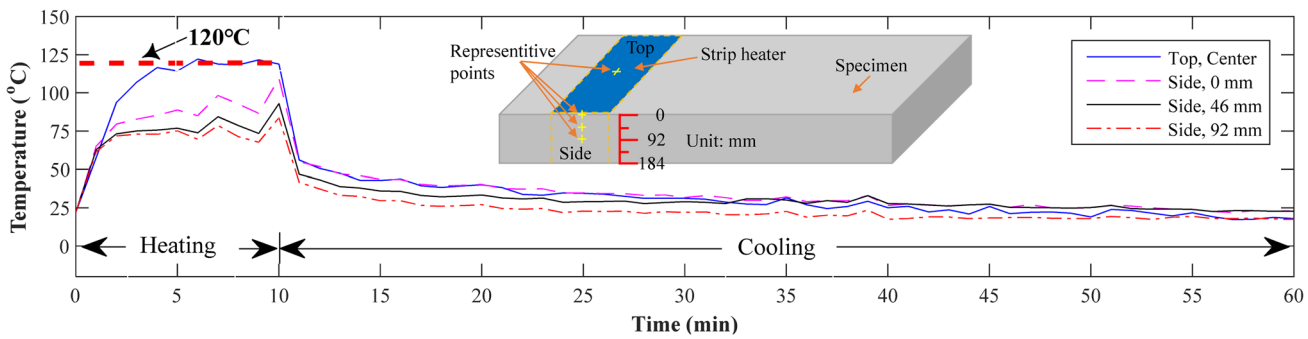

Fig. 7 Temperature variation measured by top- and side-view thermal cameras

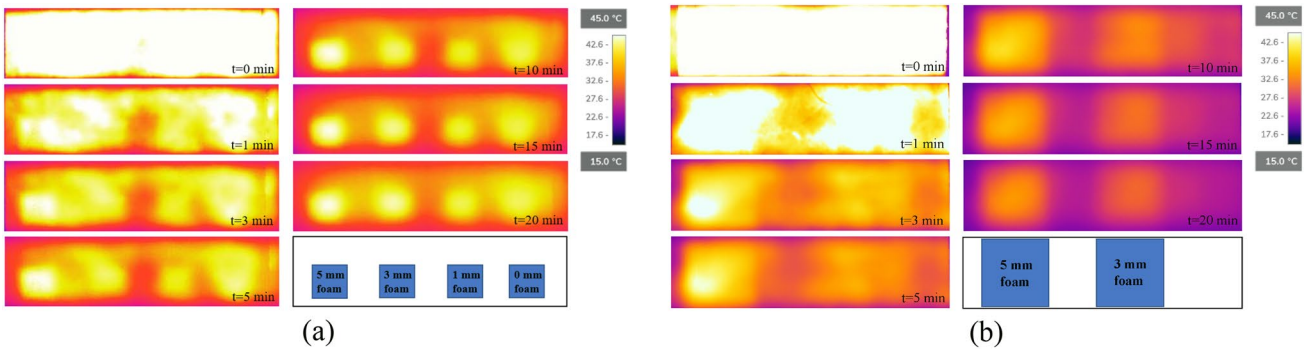

Fig. 8 Typical temperature distributions at different times in the cooling phase around delamination: **a** A–D, and **b** E–F

collection period at the cooling stage is set to 20 min in the remaining tests.

Figure 8 presents the typical temperature distribution of the delamination area over time after the strip heater is removed. The time intervals shown are 0 min, 1 min, 3 min, 5 min, 10 min, 15 min, and 20 min in the cooling phase. As expected, the delamination area exhibits a warmer temperature compared to the sounding area due to heat trapped in the cavity during heating phase and gradually fade out in the cooling phase, enabling qualitative differentiation between the damaged and sound regions. The delamination area becomes more distinctive over time till approximately 10 min. For delamination A–D represented by rectangular defects, as shown in Fig. 8a, small individual defects cannot be separated from the temperature distribution prior to $t = 5$ min. This is likely attributed to the existence of the plastic board, which increases the thickness and the heat insulation of the delamination. By the time $t = 10$ min, individual rectangular defects can be seen clearly. At $t = 20$ min, each small delamination defect (foam) appears in an elliptical shape and its corners are no longer discernible in the temperature plots. The blur effect of edges is mainly generated by the heat diffusion process [41]. Similar trends are observed from large delamination defects in Fig. 8b, which is embedded at the same depth of 25 mm (1.0 in). These findings emphasize the evolution of the thermal response of the delamination area over time, offering valuable insights into the detection process using IRT methods.

To better understand the impact of the thickness of the embedded delamination, the temperature distributions along the centerlines (both x and y directions) of the specimens at various times in the cooling phase for delamination A–D and A′–D′ in S-1, as shown in Fig. 9, were examined. It can be observed that temperature difference ΔT increases with the thickness of delamination in all but delamination D, which exhibits a slightly higher temperature than delamination C before $t = 15$ min. At $t = 20$ min, the temperature of delamination D becomes lower than that of delamination C. This behavior may be attributed to the non-uniform heating of the strip heater caused by the uneven concrete surface. At 3 min, the heat trapped in the delamination area is higher than that in the sounding area. As the cooling process progresses up to 20 min, the distribution of ΔT tends to become uniformly distributed across the specimen. The profile of ΔT can reflect the delamination shape in both x and y directions, but the error increases with an increase in embedded depth. This effect is likely due to the heterogeneity of the concrete and the longer distance in the heat transfer path. Overall, the study highlights how delamination thickness influences the thermal propagation, providing valuable insights into the detection process using passive IRT.

Similar to the observation on small delamination, the temperature difference ΔT increases with the increase in thickness for large delamination, as seen in Fig. 10. The temperature contrast is higher near the edges of the delamination area during the initial cooling period, up to 5 min. However, as the cooling process continues, the temperature distribution stabilizes between 10 and 20 min. The temperature distribution effectively reflects the size of the delamination for both E–F and E′–F′. These findings provide valuable insights into how delamination thickness affects the thermal response during passive IRT and can aid in quantifying the size and extent of large delamination.

4.2 Passive IRT

Figure 11 presents the bridge deck images captured using visible and thermal imagers. In Fig. 11a, a three-color tarp was set up to explore the impact of color variation on temperature changes in the thermal image. Correspondingly, Fig. 11b demonstrates that the darker areas in the RGB image in Fig. 11a exhibit a warmer color in the thermal image. This occurs because the dark surfaces absorb more solar energy, which is then converted into heat and detected by the thermal imager. Similar to the delamination area, the accidental oil stains (highlighted in an ellipse in the lower right corner) on the right side of S4 during transportation

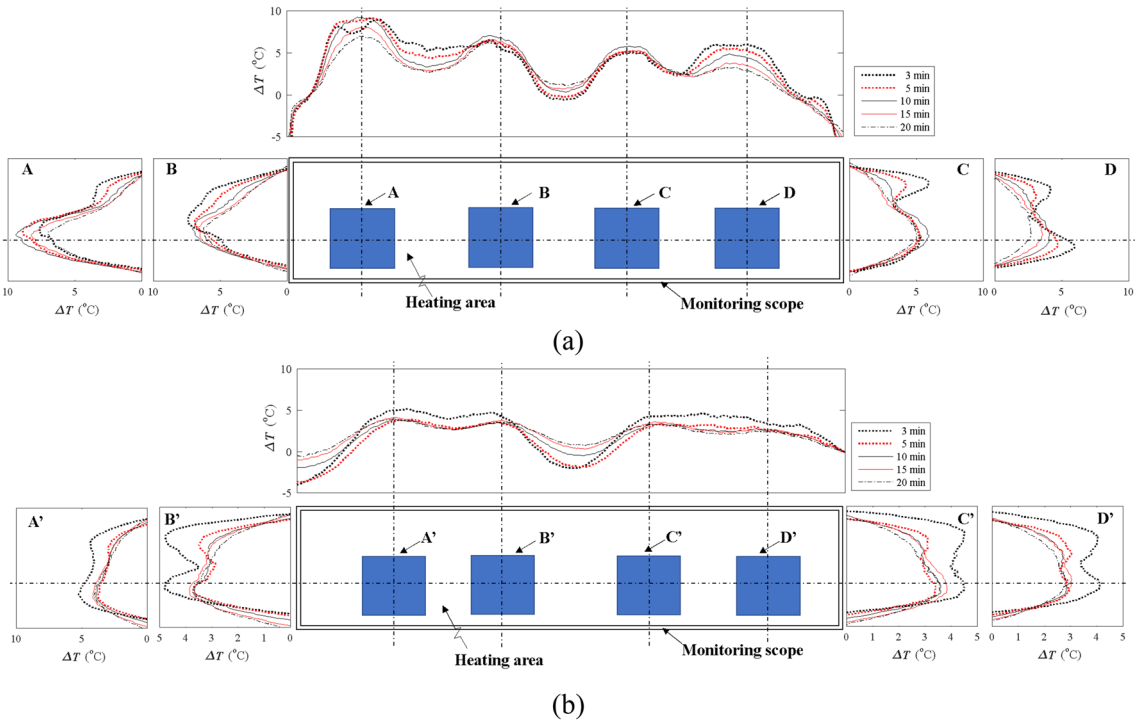

Fig. 9 Typical temperature evolutions over time in the cooling phase along the centerlines (both x and y directions) of small delamination: **a** A–D, and **b** A'–D'

from indoor to outdoor also exhibit a warmer color. Additionally, higher temperatures are observed in the areas near the gaps between S2 and S3 and between S3 and S4 (highlighted in the other two ellipses).

To mitigate these effects, data fusion utilizing both RGB and thermal images is necessary. Upon closer examination, it is evident that the large delamination area (highlighted by a large solid square) can be distinguished from the sound area, as it appears in a warmer color. However, small delamination areas (highlighted by small dashed squares) cannot be easily differentiated due to the relatively lower temperature difference between the delamination and sound areas. These observations agree well with those found by Vaghefi [42], which signifies the importance of data fusion and careful analysis of visible and thermal images to accurately detect and distinguish various types of delamination on bridge decks.

5 Discussion

The experimental results obtained from the active and passive IRTs are based to further discuss three important subjects. These subjects are the effects of delamination thickness, depth, and size; comparison of temperature distribution; and comparison of delamination size detection.

5.1 Effects of delamination thickness, depth, and size

Figure 12 and Fig. 13 present the statistical results of thermal contrasts for small and large delamination during the cooling phase. In Fig. 12a, for delamination A with a styrofoam thickness of 5 mm, ΔT initially increased and then decreased with cooling time. However, the mean ΔT kept increasing with cooling time for delamination B and C, which have a smaller styrofoam thickness of 3 mm and 1 mm, respectively. For the smallest delamination denoted as D, the mean ΔT remains almost constant. Figure 12b shows that the coefficient of variation (CV) of thermal contrasts decreased with the delamination thickness and the cooling time for delamination A, B, and C. The CV for delamination D is almost constant. As shown in Fig. 13a, the varying trend of the thermal contrast is similar for cases with the same concrete cover thickness, but the initial temperature is higher for thicker delamination. For delamination with 150 mm length and 25 mm depth as the critical parameters defined by AASHTO when their thickness ranges from 1 to 5 mm, the average temperature difference is more than 2 ℃, which is significantly larger than the effective detection temperature band that is 0.2–0.4 ℃ reported in the literature [26, 43]. In addition, the detection rate and quantification of the delamination with 150 mm length can be significantly

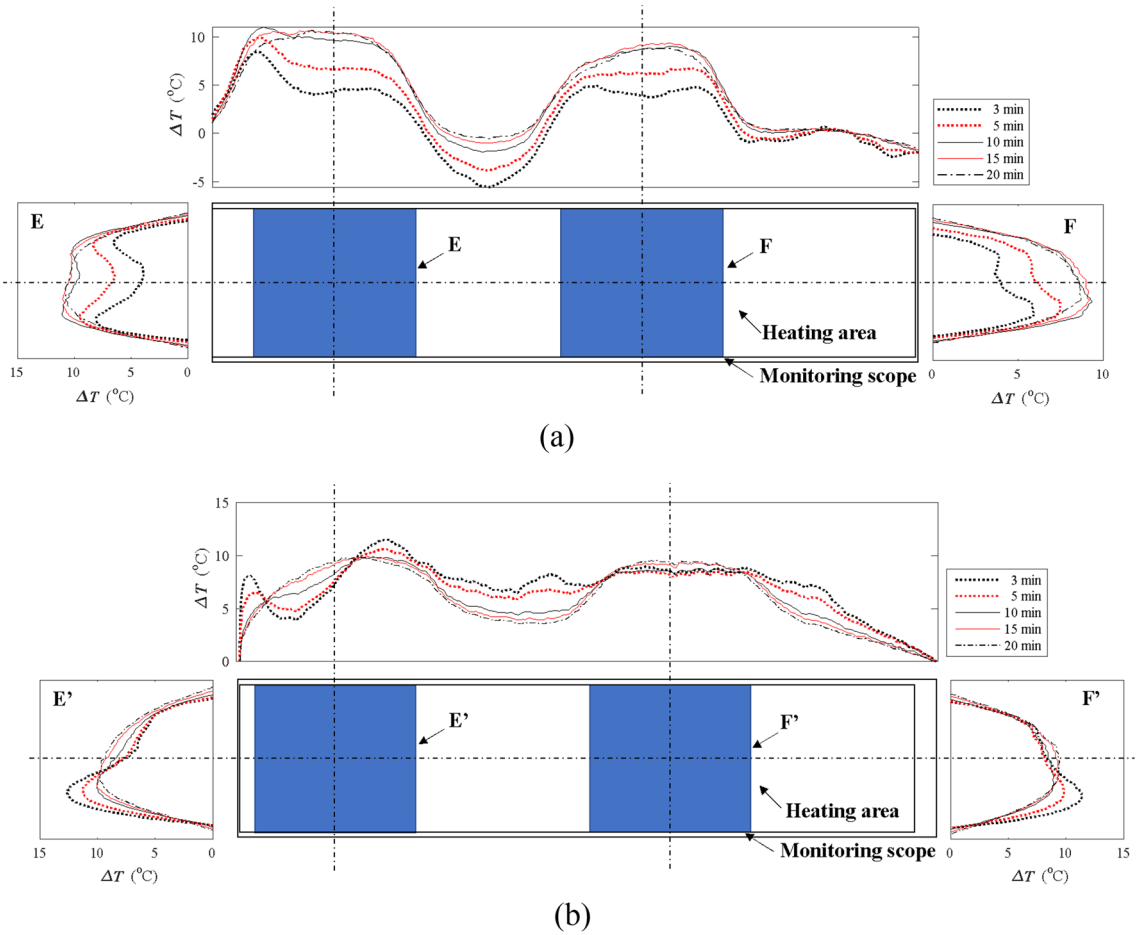

Fig. 10 Typical temperature evolutions over time in the cooling phase along the centerlines (both x and y directions) of small delamination: **a** E–F, and **b** E'–F'

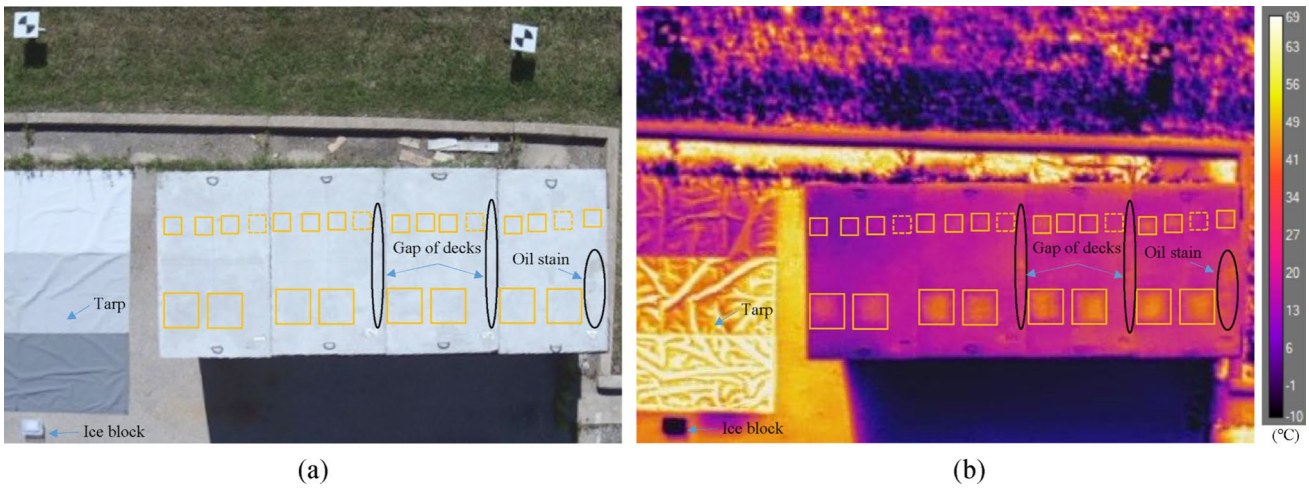

Fig. 11 Data collection through a drone: **a** RGB; and **b** thermal image

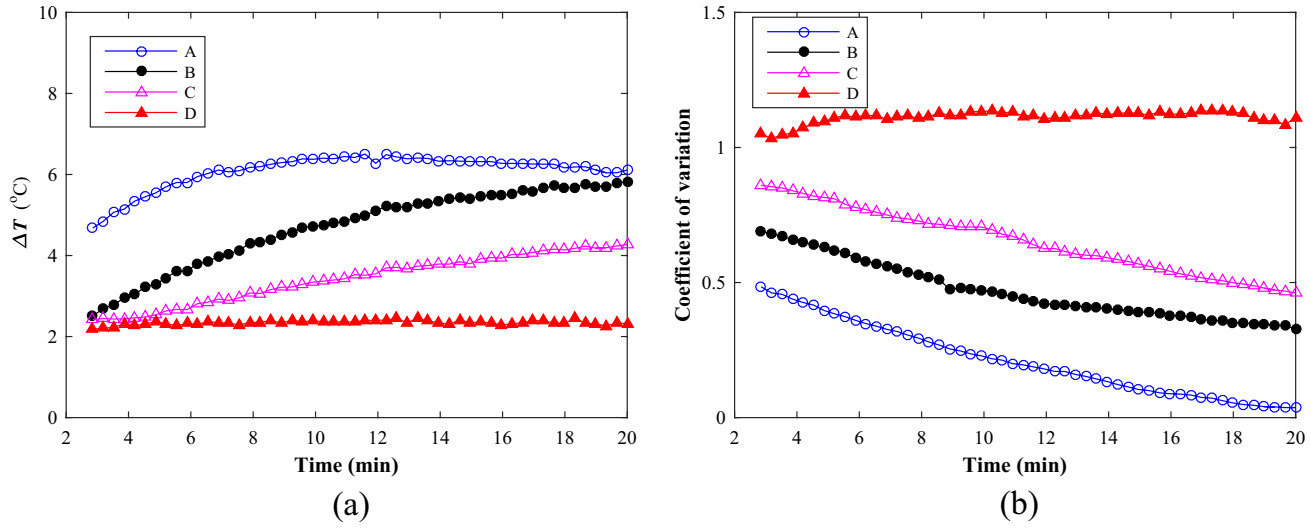

Fig. 12 Statistical variation of ΔT for small delamination in four slabs during cooling phase: **a** mean, and **b** CV

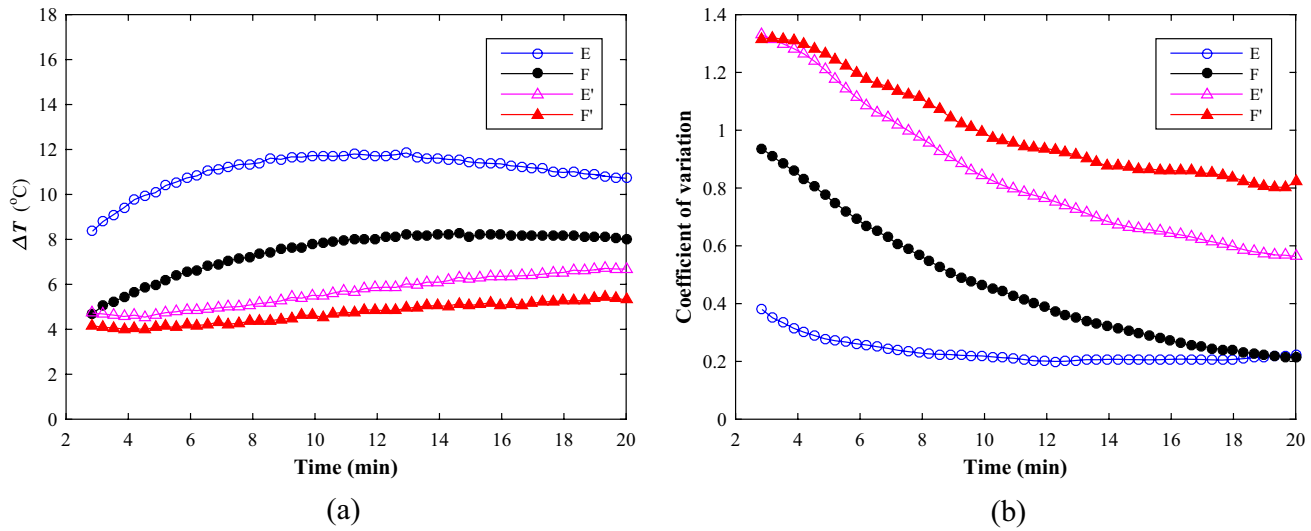

Fig. 13 Statistical variation of ΔT for large delamination in four slabs during cooling phase: **a** mean, and **b** CV

improved, with the help of advanced thermal image processing method, such as attention-based generative adversarial network with internal damage segmentation [44].

For delamination E and F, embedded at 25 mm depth, the mean time to reach the maximum ΔT is approximately 13 min for both 5 mm and 3 mm foams. However, for delamination E' and F', which are 38 mm deep into the concrete, the mean time at maximum ΔT increased to approximately 20 min for both 5 mm and 3 mm foams. Figure 13b illustrates the CV of the thermal contrast for large delamination in all four RC slabs during the cooling stage. The CV for all cases decreases with the increase in cooling time. The thicker the embedded depth and the thinner the delamination thickness, the higher the CV. This indicates that it is more accurate to detect shallower and thicker delamination defects.

Overall, the mean thermal contrasts increase with the delamination thickness and size but decrease with the embedded depth, based on the test results using the active IRT method. These results are consistent with numerical findings obtained by Hiasa et al. [26] and Maierhofer et al. [45]. The CV of thermal contrasts decreases with time or

remains nearly constant over time. Additionally, the CV is higher when the thermal contrast is higher, which can be attributed to the heterogeneity of concrete and the variation of ambient temperature. These findings provide valuable insights into the thermal response of delamination during the cooling phase and can aid in effective detection and analysis using passive IRT.

5.2 Comparison of temperature distribution

Figure 14 compares the temperature distributions obtained from active calibration tests and UAV-based passive IR sensing. As expected, the temperature of the delamination area is higher in both active and passive sensing results. However, for the active IR method, as shown in Fig. 14a, the test results for all four slabs consistently show that the temperature of the delamination area increases with the delamination thickness. For the passive IR method, as presented in Fig. 14b, this rule is not always followed. For example, S-1 and S-3 exhibit an opposite trend, which might be influenced by factors such as wind effects or the relatively small amplitude of ΔT in passive sensing. For S-3, the delamination of foams with spacings of 3.8 mm and 2.5 mm can be distinguished by both active and passive IRTs. However, this phenomenon is not observed in the other specimens, possibly due to the heterogeneity of the concrete. These findings suggest that, while both active and passive IR sensing methods can detect delamination, they may respond differently to various factors and concrete heterogeneity. Careful analysis and data fusion between the two methods are required to ensure accurate and reliable delamination detection on bridge decks using UAV-based passive IR sensing. Therefore, the UAV-based passive IRT method can be combined with the active IRT method to derive at satisfactory solutions in real-world bridge inspection. In this case, the first step is to localize the delamination area from the passive IRT method. The second step is to determine the depth and thickness of the delamination using the active IRT method.

5.3 Comparison of delamination size detection

To further evaluate the performance of UAV-based passive IR methods, the temperature gradient amplitude obtained from the gradient method, as presented in Eqs. (6) and (7), was adopted. Figure 15a illustrates that most of the small delamination can be distinguished from the sound areas using the active IR method with a pixel density of 3.66 pixel/cm (9.29 pixel/inch). However, one small delamination denoted as C in S4 cannot be found in the image, likely due to an unexpected placement during concrete casting.

The boundary of the strip heater covered area can also be distinguished, owing to the temperature difference between the inside and outside of the area covered by the strip heater. On the other hand, Fig. 15b shows the temperature gradient amplitude image of the RC deck obtained from the passive

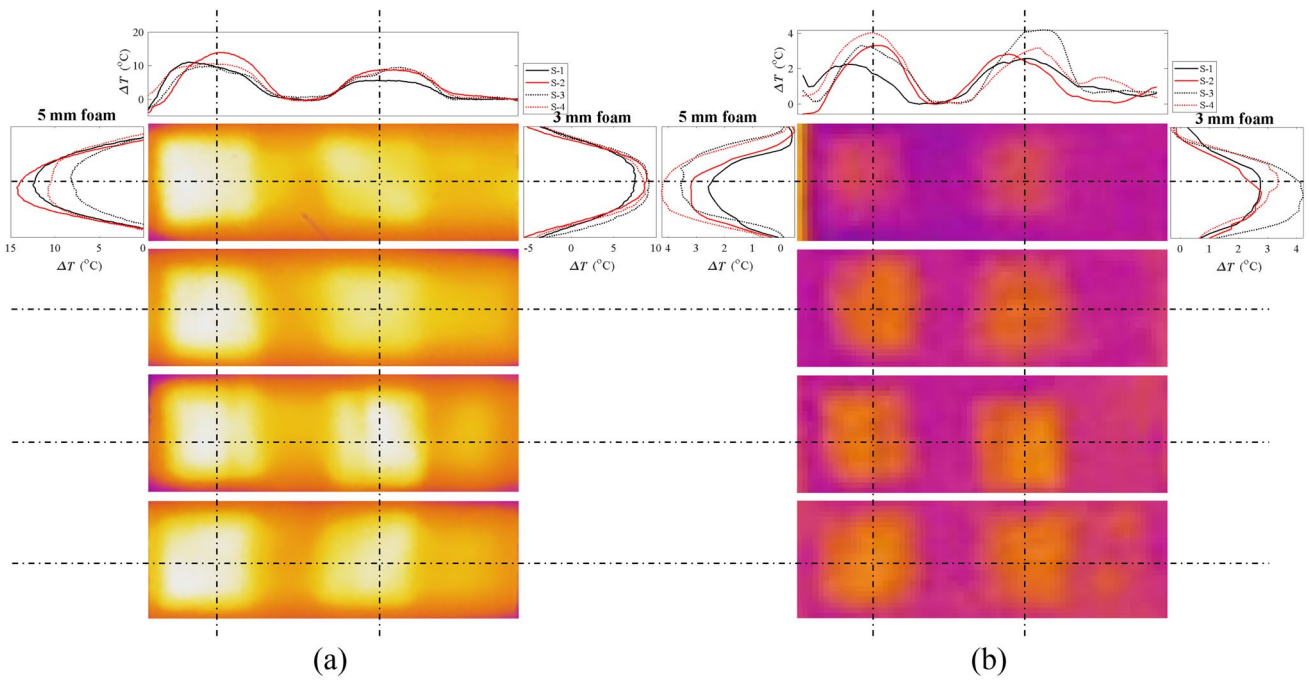

Fig. 14 Temperature distribution along the centerlines of large delamination E–F in x and y directions at 10 min, obtained by: **a** Active, and **b** passive IRT

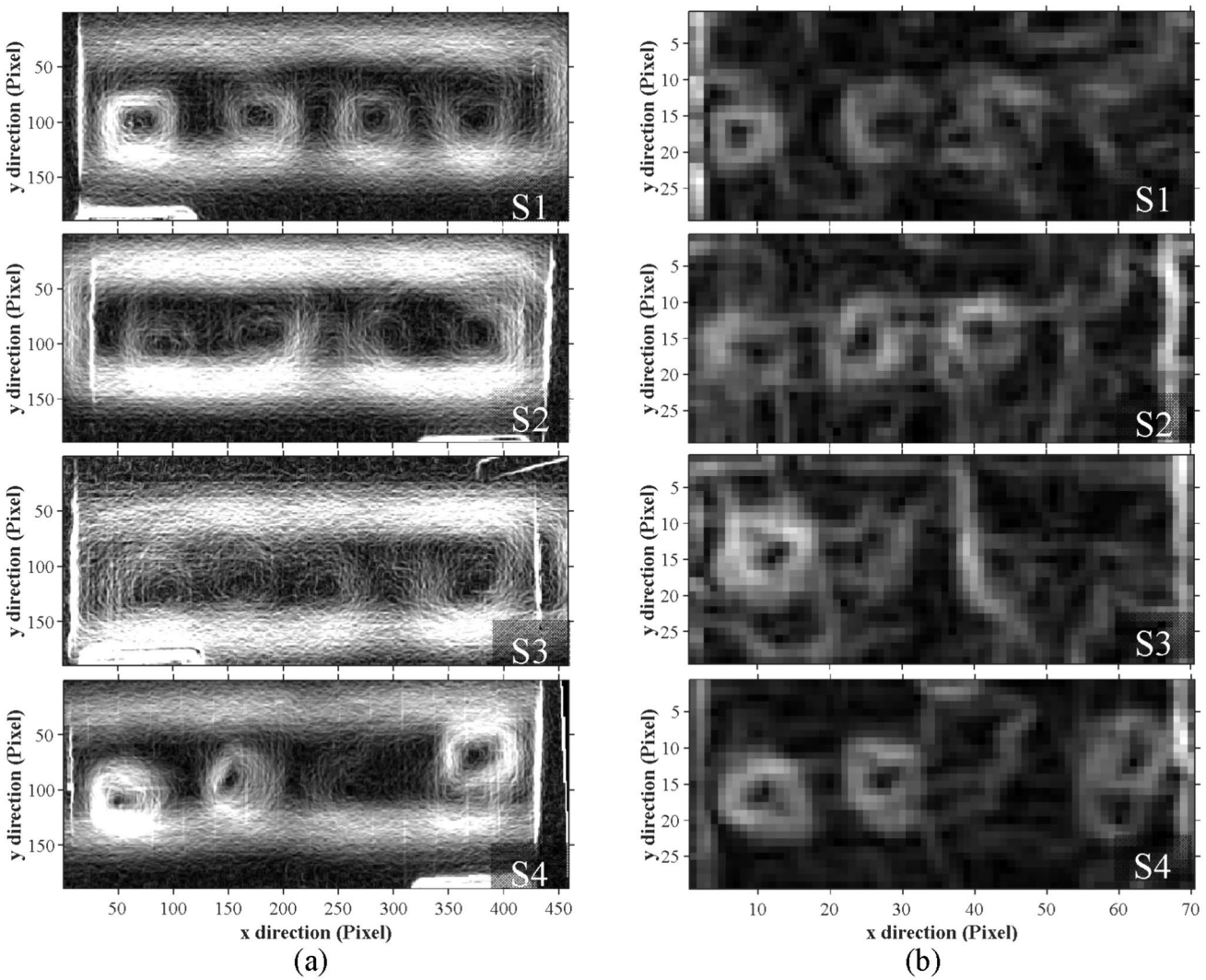

Fig. 15 Temperature gradient amplitude images for the detection of small delamination A–D in S1–4 using **a** active, and **b** passive IRT

IR method with a pixel density of 0.63 pixel/cm (1.6 pixel/inch). In this image, the small delamination C in S4 cannot be found. The small delamination D in S1 ~ S3, while detectable using the active IR method, cannot be detected either using the passive IR method. This might be due to the combined effects of the lower pixel density of the passive IR method and the non-uniform color distribution of concrete deck surfaces induced by the ambient temperature.

These observations highlight the differences in delamination detection capabilities between the active and passive IR methods and emphasize the importance of careful consideration when selecting the appropriate method based on the specific inspection requirements and environmental conditions.

Figure 16 demonstrates the detection of large delamination located close to the top concrete surface using both active and passive IR methods. In Fig. 16a, the thicker foam shows a clearer boundary using the active IRT method, indicating a higher temperature in the area enclosed by the boundary. This suggests that the active method provides better resolution and higher thermal contrast for detecting large delamination on the bridge slabs. Figure 16b presents the gradient amplitude of large delamination detected by the passive IRT method. The outline of the large delamination defects can be seen with lower resolution in comparison with the active IRT method. This lower resolution can be attributed to the lower thermal contrast and the longer distance between the camera and the bridge decks in the passive method. Overall, both active and passive IR methods can detect large delamination near the top concrete surface. However, the active method provides higher resolution and better detection sensitivity due to the direct heating of the RC slabs. The passive IR method is influenced by

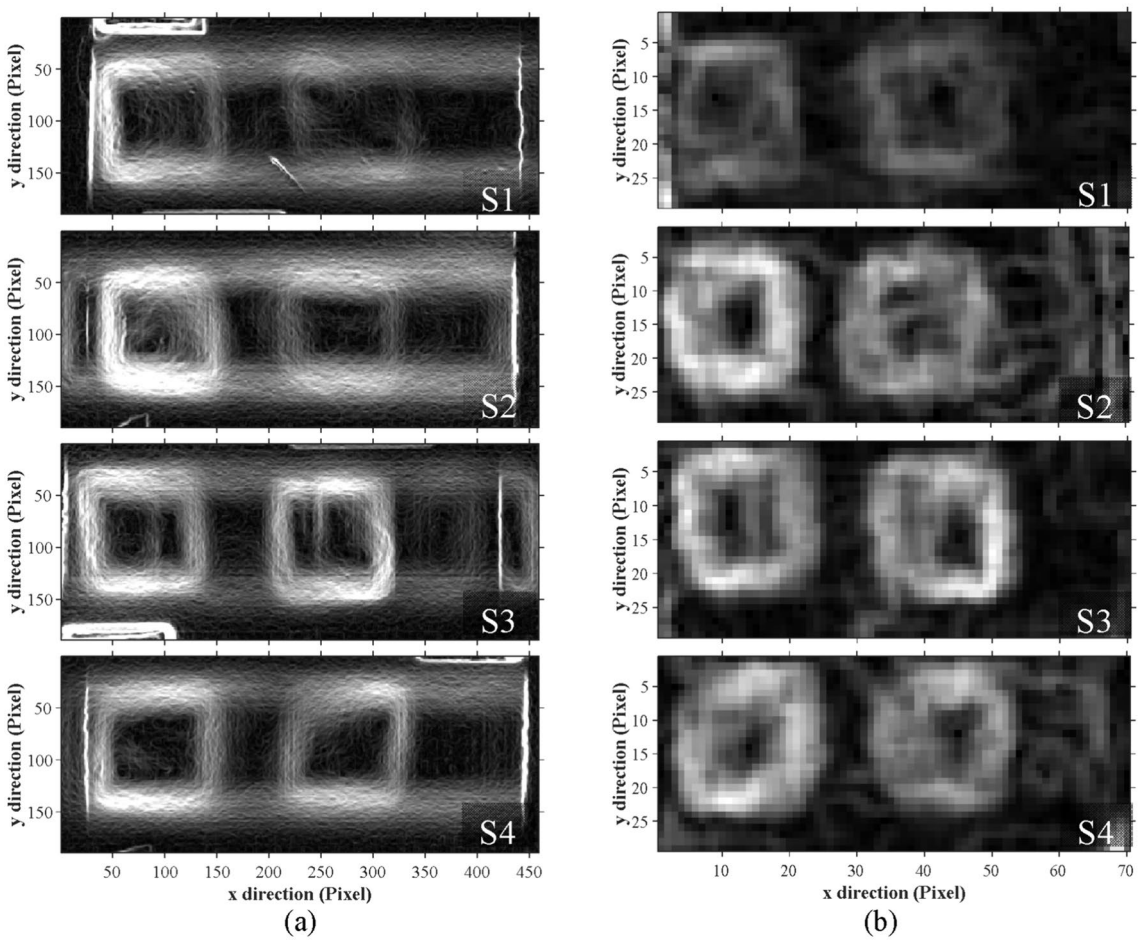

Fig. 16 Temperature gradient amplitude images for the detection of large delamination E–F in S1–4 using **a** active, and **b** passive IRT

Table 5 Comparison of delamination detection results between active and passive IR methods

	Method	Value	Small delamination				Large delamination	
			A	B	C	D	E	F
Damaged area (cm^2)	Active	Mean	201.5	200.4	197.0	195.9	932.4	910.2
		SD	9.5	10.2	18.8	14.5	7.2	15.3
	Passive	Mean	197.1	185.2	166.7	N/A	996.2	998.6
		SD	29.1	36.2	27.5	N/A	34.9	28.7
Error (%)	Active	Mean	12.8	13.3	14.4	15.2	0.2	2.2
		SD	4.1	4.4	8.1	6.3	0.8	1.6
	Passive	Mean	14.7	19.8	27.8	N/A	7.1	7.3
		SD	12.6	15.6	11.9	N/A	3.8	3.1

SD standard deviation

environmental factors and may exhibit lower resolution and thermal contrast.

Table 5 presents the measurement results of the deteriorated area and a comparison between the active and passive methods for delamination detection. It is evident that the passive method is not as precise as the active method, but the measurement errors and standard deviations (SD) are acceptable. For small delamination with an area of 232 cm^2 (1/4 ft^2), the mean monitoring error ranges from 10.4% to 15.2% for active IRT, and from 14.7% to 27.8% for passive IRT. Similarly, for large delamination with an

area of 930 cm^2 (1 ft^2), the mean measurement errors for detecting delamination E and F are, respectively, 0.2% and 2.2% using the active IR method, and 7.3% and 7.1% using the passive IR method. The maximum errors of SD for small and large delamination defects are 15.6% and 3.8% for the passive IR method, and 8.1% and 1.6% for the active IR method. With an increase in delamination thickness, the mean error also increases for both small and large delamination defects.

6 Conclusions

This study investigated the effectiveness of UAV-based passive infrared thermography (IRT) for timely detection of small and large delamination in a RC bridge deck by comparing the IRT results with those obtained from controllable indoor active IRT calibration tests of the corresponding four RC slabs. Different delamination thicknesses, sizes, spacings, and embedded depths were considered to facilitate statistical analysis. Thermal contrast and gradient amplitude of collected thermal images were employed to assess the reliability of delamination detection. Based on the experimental results and extensive statistical analyses, the following conclusions can be drawn:

1. Based on the active IRT results, the mean thermal contrast of the four RC slabs increased with the delamination thickness and size but decreased with the delamination depth. These findings confirm the numerical studies by Hiasa et al. [22] and Maierhofer et al. [38]. The CV of ΔT decreased with cooling time or remained nearly constant over time. The CV is higher when the ΔT is larger.
2. In the active IRT, the temperatures of the delamination area were consistently higher than those in the sound area, both increasing with the delamination thickness. In the passive IRT, this relationship was not always observed. Nevertheless, both the active and passive IRT methods successfully localized delamination and identified an equivalent thicknesses of as low as 1.63 mm and a size (250 mm in length or 25 mm in depth) classified as 'fair' according to the AASHTO Manual for Bridge Element Inspection.
3. The mean monitoring error of the gradient-based edge detection method to quantify the AASHTO-specified 'fair' delamination state increased with the decrease of both delamination thickness and size. The monitoring error of the UAV-based passive IRT method ranged from 14.7% to 27.8%, corresponding to a delamination thickness from 5.63 mm to 1.63 mm. However, for the active IRT method, the error ranged from 12.8% to 15.2% when the equivalent thickness decreased from 5.63 to 0.63 mm. The maximum errors in standard deviation for small and large delamination detections were 15.6% and 3.8% from the passive IRT method, and 8.1% and 1.6% from the active IRT method.
4. It is recommended that the UAV-based passive IRT method is combined with the active IRT method to establish a two-step delamination detection procedure in practice: rapid screening and refined assessment. The two-step delamination monitoring strategy has an acceptable accuracy for the evaluation of engineering parameters within application ranges as defined in the AASHTO Manuals of Bridge Element Inspection.

Acknowledgements Financial support to complete this study was provided in part by the U.S. Department of Transportation, Office of the Assistant Secretary for Research and Technology (USDOT/OST-R) under Award No. 69A3551747126 through INSPIRE University Transportation Center (https://inspire-utc.mst.edu) at Missouri University of Science and Technology and by the U.S. National Science Foundation under Award No. ECCS-2026357. In addition, this study also received joint financial support from the Hainan Provincial Science and Technology Talent Innovation Project (grant no: KJRC2023L02), and Hainan Provincial Natural Science Foundation of China (grant no: 524MS029). The views, opinions, findings, and conclusions reflected in this publication are solely those of the authors and do not represent the official policy or position of the sponsors.

Author contributions Zhang, H. B. conceived and designed the methods, conducted experiments, and prepared and wrote the manuscript; Shi, Z. H. collected test data and contributed to manuscript writing; Li, L. J. conceived the experimental methods; Jiao, P. designed the experimental specimens and collected test data; Shang, B. collected the field test data; Chen, G. acquired the research funding, supervised the research, and reviewed and edited the manuscript. All authors have read and agreed to the published version of the manuscript.

Funding Office of the Assistant Secretary for Research and Technology, 69A3551747126, Genda Chen, Key Research and Development Project of Hainan Province, KJRC2023L02, Haibin Zhang.

Data availability Data will be made available on request.

Declarations

Conflict of interest The authors declare no conflict of interest.

References

1. Black AP 2022 Bridge report. American road and transportation builders association 2022 https://artbabridgereport.org/reports/2022-ARTBA-Bridge-Report.pdf (Access on 13/09/2023)
2. Gucunski N, Imani A, Romero F, Nazarian S, Yuan D, Wiggenhauser H, Shokouhi P, Taffe A, Kutrubes D (2012) Nondestructive testing to identify concrete bridge deck deterioration. Proceeding of 92nd Annual Meeting of TRB, SHRP 2 Report. Transportation Research Board, Washington D.C.

3. Gucunski N, Ghasemi H, Maher A (2011) Condition monitoring of concrete bridge decks through periodical NDE using multiple technologies. Smart Monit, Assess Rehabilitat Civil Struct-SMAR 2011:1–9
4. America's 2021 infrastructure report card 2021 https://infrastructurereportcard.org. (Access on 09/09/2023)
5. Thompson PD, Ellis RM, Hong K, Merlo T (2003) Implementation of Ontario bridge management system. 9th International bridge management conference. Transport Research Circular, Orlando Florida, pp 112–127
6. Tran QH, Huh J, Kang C, Lee BY, Kim I, Ahn J (2018) Detectability of subsurface defects with different width-to-depth ratios in concrete structures using pulsed thermography. J Nondestr Eval 37:1–11
7. Graybeal BA, Phares BM, Rolander DD, Moore M, Washer G (2002) Visual inspection of highway bridges. J Nondestr Eval 21(3):67–83
8. Dorafshan S, Maguire M (2018) Bridge inspection: Human performance, unmanned aerial systems and automation. J Civ Struct Health Monit 8:443–476
9. Kylili A, Fokaides PA, Christou P, Kalogirou SA (2014) Infrared thermography (IRT) applications for building diagnostics: a review. Appl Energy 134:531–549
10. Pozzer S, Pravia ZMC, Rezazadeh Azar E, Dalla Rosa F (2020) Statistical analysis of favorable conditions for thermographic inspection of concrete slabs. J Civ Struct Health Monit 10(4):609–626
11. Ellenberg A, Kontsos A, Moon F, Bartoli I (2016) Bridge deck delamination identification from unmanned aerial vehicle infrared imagery. Autom Constr 72:155–165
12. Omar T, Nehdi ML (2017) Remote sensing of concrete bridge decks using unmanned aerial vehicle infrared thermography. Autom Constr 83:360–371
13. Duque L, Seo J, Wacker J (2018) Bridge deterioration quantification protocol using UAV. J Bridge Eng 23(10):4018080
14. Seo J, Duque L, Wacker J (2018) Drone-enabled bridge inspection methodology and application. Autom Constr 94:112–126
15. Cheng C, Shang Z, Shen Z (2019) Bridge deck delamination segmentation based on aerial thermography through regularized grayscale morphological reconstruction and gradient statistics. Infrared Phys Technol 98:240–249
16. Ding W, Yang H, Yu K, Shu J (2023) Crack detection and quantification for concrete structures using UAV and transformer. Autom Constr 152:104929
17. Shu J, Ding W, Zhang J, Lin F, Duan Y (2022) Continual-learning-based framework for structural damage recognition. Struct Control Health Monit 29(11):e3093
18. Cui Z, Wang Q, Guo J, Lu N (2022) Few-shot classification of façade defects based on extensible classifier and contrastive learning. Autom Constr 141:104381
19. Jeong E, Seo J, Wacker J (2020) Literature review and technical survey on bridge inspection using unmanned aerial vehicles. J Perform Constr Facil 34(6):4020113
20. Ali R, Kang D, Suh G, Cha Y (2021) Real-time multiple damage mapping using autonomous UAV and deep faster region-based neural networks for GPS-denied structures. Autom Constr 130:103831
21. AASHTO (2019) Manual for bridge element inspection, In: American association of state highway and transportation officials
22. Raja BNK, Miramini S, Duffield C, Sofi M, Zhang L (2022) Infrared thermography detection of delamination in bottom of concrete bridge decks. Struct Control Health Monit. 29(3):e2886. https://doi.org/10.1002/stc.2886
23. Zou X, Wang L, Wang J, Liu J, Ma H, Bao Y (2022) Nondestructive evaluation of carbon fiber reinforced polymer (CFRP)-steel interfacial debonding using eddy current thermography. Compos Struct 284:115133
24. Mac VH, Tran QH, Huh J, Doan NS, Kang C, Han D (2019) Detection of delamination with various width-to-depth ratios in concrete bridge deck using passive IRT: limits and applicability. Materials (Basel) 12(23):3996
25. Hiasa S, Birgul R, Catbas FN (2017) Effect of defect size on subsurface defect detectability and defect depth estimation for concrete structures by infrared thermography. J Nondestr Eval 36(3):57
26. Hiasa S, Birgul R, Catbas FN (2017) Investigation of effective utilization of infrared thermography (IRT) through advanced finite element modeling. Constr Build Mater 150:295–309. https://doi.org/10.1016/j.conbuildmat.2017.05.175
27. Farrag S, Yehia S, Qaddoumi N (2016) Investigation of mix-variation effect on defect-detection ability using infrared thermography as a nondestructive evaluation technique. J Bridge Eng 21(3):4015055. https://doi.org/10.1061/(ASCE)BE.1943-5592.0000779
28. Washer G, Fenwick R, Bolleni N (2010) Effects of solar loading on infrared imaging of subsurface features in concrete. J Bridge Eng 15(4):384–390
29. Yehia S, Abudayyeh O, Nabulsi S, Abdelqader I (2007) Detection of common defects in concrete bridge decks using nondestructive evaluation techniques. J Bridge Eng 12(2):215–225. https://doi.org/10.1061/(ASCE)1084-0702(2007)12:2(215)
30. Madding RP (1983) Science behind thermography. SPIE, pp 2–9
31. Carslaw HS, Jaeger JC (1959) Conduction of heat in solids. Oxford University Press
32. Ichi E, Dorafshan S (2022) Effectiveness of infrared thermography for delamination detection in reinforce dconcrete bridge decks. Autom Constr 142:104523
33. ASTM (2022) Standard test method for detecting delaminations in bridge decks using infrared thermography. ASTM, pp 4788–03
34. Washer G, Fenwick R, Bolleni N, Harper J (2009) Effects of environmental variables on infrared imaging of subsurface features of concrete bridges. Transp Res Rec 2108(1):107–114. https://doi.org/10.3141/2108-12
35. Omar T, Nehdi ML, Zayed T (2018) Infrared thermography model for automated detection of delamination in RC bridge decks. Constr Build Mater 168:313–327
36. Barreira E, de Freitas VP (2007) Evaluation of building materials using infrared thermography. Constr Build Mater 21(1):218–224. https://doi.org/10.1016/j.conbuildmat.2005.06.049
37. Cheng C, Cheng T, Chiang C (2008) Defect detection of concrete structures using both infrared thermography and elastic waves. Autom Constr 18(1):87–92
38. Tomita K, Chew MYL (2022) A review of infrared thermography for delamination detection on infrastructures and buildings. Sensors (Basel) 22(2):423
39. Wiecek B (2006) Review on thermal image processing for passive and active thermography, in Proceeding of the 2005 Engineering in Medicine and Biology 27th Annual Conference. IEEE, Shanghai
40. Prewitt JM (1970) Object enhancement and extraction. Pict Process Psychopictorics 10(1):15–19
41. Wu J, Zhu J, Xia H, Liu C, Huang X, Tian GY (2019) DC-biased magnetization based eddy current thermography for subsurface defect detection. IEEE Trans Industr Inform 15(12):6252–6259
42. Vaghefi K (2013) Infrared thermography enhancements for concrete bridge evaluation. Michigan Technological Univesity Houghton, MI, USA, Ph.D.
43. Clark MR, Mccann DM, Forde MC (2003) Application of infrared thermography to the non-destructive testing of concrete and masonry bridges. Ndt E Int 36(4):265–275. https://doi.org/10.1016/S0963-8695(02)00060-9
44. Ali R, Cha Y (2022) Attention-based generative adversarial network with internal damage segmentation using thermography. Autom Constr 141:104412
45. Maierhofer C, Brink A, Röllig M, Wiggenhauser H (2005) Quantitative impulse-thermography as non-destructive testing method in

civil engineering—experimental results and numerical simulations. Constr Build Mater 19(10):731–737. https://doi.org/10.1016/j.conbuildmat.2005.06.002

Publisher's Note Springer Nature remains neutral with regard to jurisdictional claims in published maps and institutional affiliations.

Springer Nature or its licensor (e.g. a society or other partner) holds exclusive rights to this article under a publishing agreement with the author(s) or other rightsholder(s); author self-archiving of the accepted manuscript version of this article is solely governed by the terms of such publishing agreement and applicable law.